Krishnaiah, KM., & Railton, CJ. (1999). A stable subgridding algorithm and its application to eigenvalue problems. *IEEE Transactions on Microwave Theory and Techniques*, *47*(5), 620 - 628. https://doi.org/10.1109/22.763164

A Stable Subgridding Algorithm and Its Application to Eigenvalue Problems

K. M. Krishnaiah and Chris J. Railton, *Member, IEEE*

***Abstract*— In this paper, a new and stable subgridding algorithm is proposed for three-dimensional problems which provides subgridding in both space and time. The concept of an equivalent-circuit representation and a novel leapfrog time integration scheme is used to ensure that the algorithm is stable and efficient. Practical applications of this algorithm in the characterization of arbitrarily filled dielectric resonators are reported.**

***Index Terms*— FDTD methods.**

I. Introduction

THE time-dependent Maxwell's differential equations can be represented by a set of difference equations and can be solved numerically on a computer. This method of solving Maxwell's equations is popularly known as the finite-difference time-domain (FDTD) method, which was first proposed in [1] for two dimensions and later applied to three dimensions in [2]–[5]. The FDTD method of solving Maxwell's equations is becoming popular mainly due to its simplicity. It has been widely and effectively used to solve a broad range of electromagnetic problems [6], [7].

In some problems, a greatly improved accuracy of solution can be obtained if a finer discretization is used in specific regions of the computational volume. Frequently, the electric or magnetic fields or both have large gradients within a limited volume or sometimes only in one direction. A brute-force approach of using a sufficiently fine grid (FG) throughout the computational volume invariably requires exceedingly large computer resources. Also, some structures have a curved boundary which needs staircase approximations, which results in loss of accuracy. In such cases, accuracy depends on the cell dimensions and usually requires small cells if the curve is sharp, which again poses the same problems of expensive computation, memory, and computer limitations.

Some methods [3], [6], [8]–[11] have been proposed to overcome the burden of excessive computer resources requirement. Some of the methods [3], [8] use large FDTD cells throughout the computation volume, but approximate the small geometry elements by modifying the equations for the large cells that contain them. For example, a surface-impedance concept may be used to include material layers thinner than the FDTD cells [8], [10]. Another variation involves special equations for calculating the fields in the vicinity of discontinuity thinner than the FDTD cell size [3], [11]. In the case of the contour path (CP) method [9], which is used for curved boundaries, the basic Cartesian grid arrangement of field components at all space cells, except those immediately adjacent to the structure surface, are preserved. Space cells adjacent to the structure surface are deformed to conform with the surface locus. Slightly modified time-stepping expressions for the field components adjacent to the surface are obtained by using the CP technique. The drawback of this method is that it has a very limited range of applicability and may exhibit longtime instability [12], [13].

In the expansion technique [6], the region of interest in the volume being analyzed is replaced with a finer grid. The technique consists of making an initial computer run with a model of the entire system. The electric fields, scattered from the system and tangential to a sub-boundary, are stored on disk from this calculation. The portion of the volume inside the sub-boundary is then subdivided into smaller cells and the sub-boundary becomes the outer boundary for a second calculation. The same tangential E-field response, as seen on the sub-boundary for the first run, is imposed on the outer boundary of the second run. The advantage of the second run with smaller grid cells is that the missing volume of the domain appears to be present at this time. A few drawbacks of this method are: 1) it assumes only weak coupling between main and sub-volume; 2) it suffers from very slow processing speed; and 3) it is mesh dependent.

A few general schemes have previously been developed for a dynamic change of the discretization density in the FDTD algorithm. They include mesh refinement in both time and space [14]–[16], and mesh refinement in space only [17]. While the latter approach is much simpler to implement, the time and space subgridding yields a much more efficient code. This results from the fact that, in the second approach, the stability condition has to be computed from the size of the smallest cell used and, thus, a small time step is needed in the whole problem space. The variable step-size method (VSSM) [15] and the mesh-refinement algorithm (MRA) [16], are similar to the proposed subgridding technique in the sense that they also make use of dividing the computational domain into two or more regions with different cell size. The disadvantage in using these methods is that both require the calculation of extra second-order difference equations at each coarse node on the boundary and also storage of an extra second-order difference—the required number of stored fields increases with the increase in the ratio of the fine and coarse cell sizes. The difference between the MRA and VSSM is that in the VSSM, the second-order differences are calculated from spatially interpolated field values, whereas in the MRA, the

Manuscript received July 22, 1997; revised November 19, 1998. The work of K. M. Krishnaiah was supported by the Commonwealth Commission, U.K.

The authors are with the Centre for Communications Research, University of Bristol, Bristol BS8 1TR, U.K.

Publisher Item Identifier S 0018-9480(99)03133-6.

second-order differences are calculated and then interpolated in space. The authors have reported [18] longtime instability in implementing these methods.

During the preparation of this paper, an alternative method was published [19] for developing a subgridding algorithm in a manner which has some similarities to the method described here. While the overall aim of [19] and of the method described here is the same, there are some differences in the approach and final algorithm. Whereas in [19] the discrete curl and divergence operators are used in the derivation, in this paper, the consistency is assured by making the subgridding algorithm formally identical with a passive electrical circuit [22], [23]. In addition, [19] assumes the boundary magnetic field $\boldsymbol{H}_{bc}$ to be constant over the coarse grid (CG) time step, whereas in the proposed method, a novel time interpolation has been implemented. These differences lead to different update equations in the final algorithm. A further difference is that in [19], a subgrid (SG) ratio of two is used, whereas in this paper, a ratio of three is used. The performance, however, of the two methods appears to be similar.

Previously, the application of this algorithm in two dimensions to characterize an arbitrarily filled dielectric waveguide has been shown [18]. The objective of the work presented in this paper is to develop a practical three-dimensional (3-D) subgridding algorithm, which is efficient and stable, and also to characterize its performance under various conditions. The entire computational volume is divided into a main grid (coarse) and a number of SG's (fine). The SG is introduced only around the discontinuities where the field gradients are high. To maintain the Courant stability criterion and minimize the dispersion, different time steps are used based on the main and SG spatial step. The fields within each grid volume, either main grid or SG, are found using standard FDTD equations.

When a FG is embedded within an CG, the boundary field components of the FG cannot be calculated using the standard FDTD equations. The field amplitudes on the CG may then be used to estimate the field amplitudes on the FG by linear or cubical splines or shape-preserving interpolations, e.g., [20]. However, a simple interpolation that does not maintain the *reciprocity* of contribution between $\boldsymbol{E}$ and $\boldsymbol{H}$ fields can lead to late time instability. The main-grid boundary fields are found based on the problem definition, i.e., metal or absorbing boundary condition (ABC). This subgridding algorithm decreases the computer resource requirements and expands the capability of FDTD to more complex problems such as thin wires, slots, posts, etc. In Section II, the concept of an equivalent circuit for a 3-D grid discontinuity is described. In Section III, the novel time interpolation method is briefly explained with the aid of a time-flow graph. In Section IV, the complete algorithm along with representative field updation equations is presented. Finally, Sections V and VI discuss the numerical results and draw conclusions.

II. An Equivalent Circuit of the Grid Discontinuity

Although a passive lumped circuit equivalent to Maxwell's equations has previously been published [21], the form of this circuit does not lend itself to the analysis of FDTD with subgridding. It is emphasized that the circuit presented here is not a lumped equivalent to some discontinuity or other physical feature to be included in the FDTD algorithm—it is an equivalent to the subgridding algorithm itself.

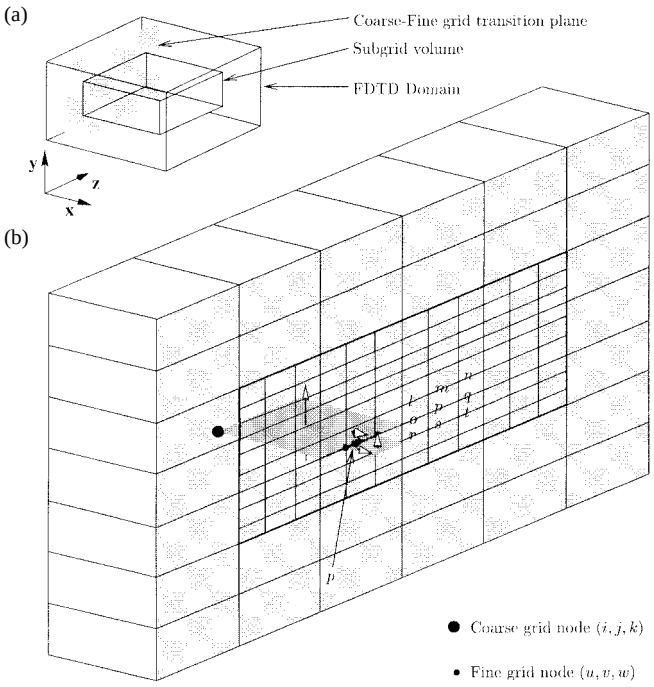

Fig. 1. A typical tangential FG boundary electric field $E_{bfz}(u, v, w+1/2)$, coupled to one CG magnetic field $H_{bcy}(i+1/2, j, k+1/2)$ and three FG magnetic field $H_{fx}(u, v-1+1/2, w+1/2), H_{fy}(u+1/2, v, w+1/2)$ components at the CG to FG transition plane.

The equivalent circuit of the unmodified Yee cell consists of gyrators, connected between $\boldsymbol{E}$ and $\boldsymbol{H}$ nodes, and capacitors at all nodes [23]. The gyrators transfer energy between $\boldsymbol{E}$ and $\boldsymbol{H}$ field nodes, whereas the capacitor at each node stores the energy. For an unmodified cell, the gyrator values are $G_x = \Delta y \Delta z$, $G_y = \Delta z \Delta x$, $G_z = \Delta x \Delta y$, and the capacitor values are $C_e = \epsilon_0 \Delta x \Delta y \, \Delta z$, $C_h = \mu_0 \Delta x \Delta y \Delta z$. In the case of the grid discontinuity equivalent circuit, the gyrator values are a function of the interpolation polynomial that will be used in the interpolation of the boundary CG magnetic field. In the case of two-dimensional problems, the gyrator values depend only on the interpolation coefficients. In 3-D problems, they depend on the interpolation coefficients in the normal direction to the field that is being interpolated and a splitting coefficient [19], which determines the contribution of the CG boundary magnetic field, in the tangential direction of the field that is being interpolated. The calculation of gyrator and capacitor values is presented in the following two sections.

A. Equivalent Circuit for the Algorithm in Three Dimensions

In [18], an equivalent circuit for the subgridding algorithm in two dimensions is presented. For the case of three dimensions, the updating scheme becomes more complicated. The schematic representation of the typical transition plane between coarse and FG is shown in Figs. 1 and 2. The exploded view of the transition plane is shown in the Figs. 1(b) and 2(b). The FDTD domain and the coordinate axes are also shown. The gyrators and capacitors are not shown for

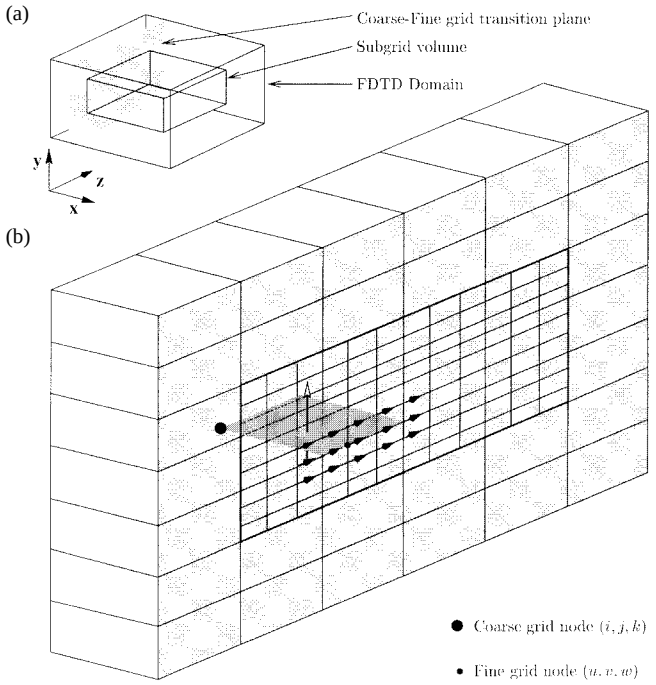

Fig. 2. A typical tangential CG boundary magnetic field $H_{bcy}(i + 1/2, j, k + 1/2)$, coupled to 15 FG electric field $E_{fz}(u, v - 1 : v + 1, w - 2 + 1/2 : w + 2 + 1/2)$ components at the coarse to FG transition plane.

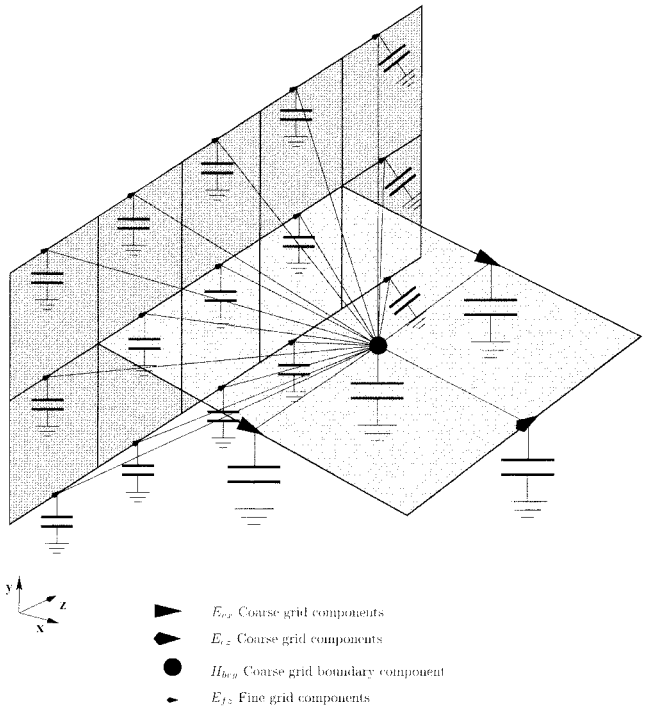

Fig. 3. Partial 3-D grid discontinuity equivalent circuit. The gyrators and capacitors connected to the CG boundary magnetic-field node and FG boundary electric-field nodes.

clarity. In Fig. 3, however, an enlarged view of one CG magnetic field node in which the gyrators and the capacitors, which are connected to the boundary FG electric field nodes, are shown. In the case of three dimensions, the gyrator values are the product of the interpolation coefficients and splitting coefficient. The interpolation coefficients determine

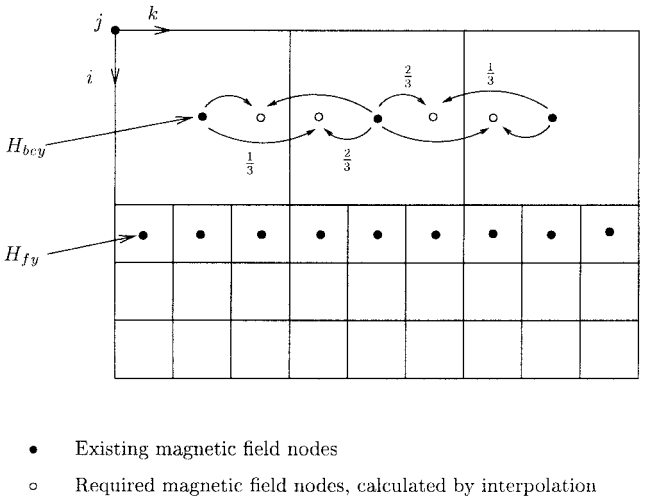

Fig. 4. Linear interpolation in the direction normal to the CG magnetic field at the transition plane.

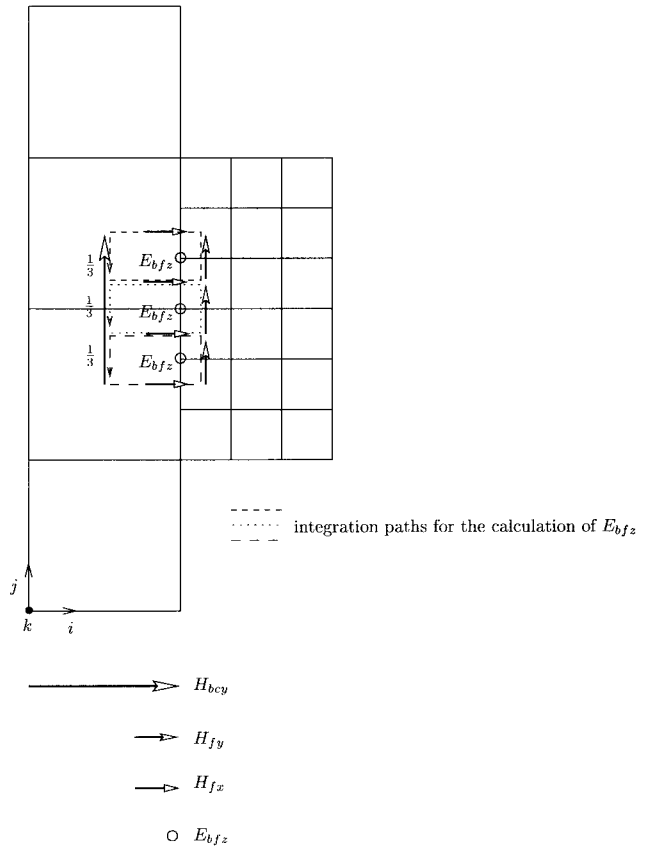

Fig. 5. Length splitting in the direction tangential to the CG magnetic field at the transition plane [19].

the contribution of the CG boundary magnetic field in the direction normal to the field component, whereas the splitting coefficients determine the contribution of the CG boundary magnetic field in the direction tangential to the field component [19]. The value of the splitting coefficient depends on the common integration path and permeability distribution.

The linear interpolation coefficients in the normal direction are shown in Fig. 4. The splitting coefficients in the tangential direction have been shown in the Fig. 5. The dotted CP of the

TABLE I
VALUES OF GYRATORS, g_{1-15}, THAT ARE CONNECTED BETWEEN TYPICAL BOUNDARY CG AND FG NODES IN THE TRANSITION PLANE [SEE (3)]

		$E_{bfz}(u, \hat{v}, \hat{w}+\frac{1}{2})$				
	$\hat{v} \setminus \hat{w}$	$w-2$	$w-1$	w	$w+1$	$w+2$
$H_{bcy}(i+\frac{1}{2}, j, k+\frac{1}{2})$	$v-1$	g_1 $\frac{1}{9}\cdot\frac{1}{3}$	g_4 $\frac{1}{9}\cdot\frac{2}{3}$	g_7 $\frac{1}{9}\cdot\frac{3}{3}$	g_{10} $\frac{1}{9}\cdot\frac{2}{3}$	g_{13} $\frac{1}{9}\cdot\frac{1}{3}$
$C_{Hbcy}=1$	v	g_2 $\frac{1}{9}\cdot\frac{1}{3}$	g_5 $\frac{1}{9}\cdot\frac{2}{3}$	g_8 $\frac{1}{9}\cdot\frac{3}{3}$	g_{11} $\frac{1}{9}\cdot\frac{2}{3}$	g_{14} $\frac{1}{9}\cdot\frac{1}{3}$
	$v+1$	g_3 $\frac{1}{9}\cdot\frac{1}{3}$	g_6 $\frac{1}{9}\cdot\frac{2}{3}$	g_9 $\frac{1}{9}\cdot\frac{3}{3}$	g_{12} $\frac{1}{9}\cdot\frac{2}{3}$	g_{15} $\frac{1}{9}\cdot\frac{1}{3}$

FG magnetic field is common to $1/3$ of the CG magnetic field. Similarly, the small dashed and big dashed CP's also have common path of $1/3$ of a CG magnetic-field component. In this configuration, the value of the splitting coefficient becomes $1/3$. The resultant gyrator values that are connected to a typical CG boundary magnetic-field node $H_{bcy}(i+1/2, j, k+1/2)$ are shown in Table I.

In this case, the entire transition plane electric-field components have to be calculated as opposed to just a line in two dimensions. Since the FG is embedded in the CG, (i, j, k) has been used as the CG coordinate system and (u, v, w) for the FG coordinate system for ease of understanding. The exact update equations for the FG boundary electric field and CG boundary magnetic field are given so that they can be directly plugged into the existing codes with little or no modification. A typical CG node are indicated by the symbol ● and a typical FG node are indicated by the symbol • in Figs. 1(b) and 2(b). CG and FG fields are also distinguished by suffix c and f.

To update the FG boundary electric field, at least one FG magnetic-field component will *always* be outside the FG boundary. This outside FG boundary magnetic field is calculated by interpolation and splitting of the CG boundary magnetic field.

The FG boundary electric field, e.g., $p = E_{bfz}(u, v, w+1/2)$ in Fig. 1, cannot be updated in the usual way because the required FG magnetic-field component $H_{fy}(u-1/2, v, w+1/2)$ does not exist. The nonexistent FG magnetic-field component is obtained by linearly interpolating the CG magnetic field in the normal direction (Fig. 4). The same CG magnetic field coupled with its neighbors is used to update the remaining eight other E_{bfz} i.e., $(l-o, q-t)$, by splitting the magnetic field in the tangential direction at the transition plane. This way, all the nonexistent FG magnetic-field components are evaluated all over the transition plane. Now the update equation for the $E_{bfz}(u, v, w+1/2)$ node is shown in (1) at the bottom of this page, where

$$\text{HYUW} = \text{obtained from Table II}$$
$$G_f = \frac{1}{9}$$
$$C_{Ebfz} = \frac{2}{9}$$

chosen such that the standard FDTD update equations for the FG are recovered.

In the above equation, G_f represents the unmodified FG gyrator value and g_1, g_2 represent the gyrator values in the equivalent circuit of the grid discontinuity. The similar update equation can be easily obtained for the other tangential boundary electric-field component E_{bfy} at the transition plane.

Now consider the update of a typical CG boundary magnetic field $H_{bcy}(i+1/2, j, k+1/2)$ shown in (2) at the bottom of the following page. It would be natural to use just the co-located FG $E_{bfz}(u, v, w+1/2$. If it is so, $EZJK$ in (2) becomes $E_{bfz}(u, v, w+1/2)$. In this case, the update equation for H_{bcy} would not depend on any of the other E_{bfz} nodes at the transition plane. This leads to a nonreciprocal situation in which, for instance, $E_{bfz}(u, v+1, w+1/2)$ depends on H_{bcy}, but not vice-versa.

$$p = \frac{\partial E_{bfz}\left(u, v, w+\frac{1}{2}\right)}{\partial t}$$
$$= \frac{1}{\epsilon}\cdot\frac{1}{C_{Ebfz}}\left[\frac{G_f H_{fy}\left(u+\frac{1}{2}, v, w+\frac{1}{2}\right) - \text{HYUW}}{\delta x} - \frac{2G_f H_{fx}\left(u, v+\frac{1}{2}, w+\frac{1}{2}\right) - 2G_f H_{fx}\left(u, v-\frac{1}{2}, w+\frac{1}{2}\right)}{\delta y}\right] \quad (1)$$

TABLE II
BOUNDARY CG MAGNETIC-FIELD CONTRIBUTIONS TO A TYPICAL TANGENTIAL FG BOUNDARY ELECTRIC-FIELD COMPONENT

E_{bfz}	C_{Ebfz}	$HYUW$	g_1	g_2
l,o,r	$\frac{2}{9}$	$g_1 H_{bcy}(i+\frac{1}{2},j,k+\frac{1}{2}) + g_2 H_{bcy}(i+\frac{1}{2},j,k-\frac{1}{2})$	$\frac{1}{9}\cdot\frac{2}{3}$	$\frac{1}{9}\cdot\frac{1}{3}$
m,p,s	$\frac{2}{9}$	$g_1 H_{bcy}(i+\frac{1}{2},j,k+\frac{1}{2})$	$\frac{1}{9}\cdot 1$	$0\cdot 0$
n,q,t	$\frac{2}{9}$	$g_1 H_{bcy}(i+\frac{1}{2},j,k+\frac{1}{2}) + g_2 H_{bcy}(i+\frac{1}{2},j,k+\frac{3}{2})$	$\frac{1}{9}\cdot\frac{2}{3}$	$\frac{1}{9}\cdot\frac{1}{3}$

As mentioned earlier, in terms of an equivalent-circuit approach, this situation *cannot* be achieved with purely passive components and must be avoided, otherwise late time instability is likely. By replacing the grid discontinuity with an equivalent circuit, which is shown partly in Fig. 3, it can be seen that, for reciprocity, the $EZJK$ must be the sum of contributions from all 15 (for this case) E_{bfz} nodes, as shown in (3) at the bottom of this page, where

$$G_c = 1.0$$
$$g_{1\to 15} = \text{obtained from the Table II}$$
$$C_{Hbcy} = \frac{1}{4}\cdot\left[3G_c + \sum_{t=1}^{15} g_t\right]$$

chosen such that the standard FDTD update equations for the CG are recovered.

In this equation, G_c is the unmodified CG gyrator value and g_t represent the gyrator values in the equivalent circuit.

At the transition plane, a tangential CG boundary magnetic-field component is coupled to 15 or 12 or ten or eight or six FG boundary electric-field components and three CG electric-field components, depending upon its location in the transition plane. Only one case has been shown in Fig. 2(b). This algorithm can easily be implemented when there is more than one SG in the problem domain and can also be implemented recursively without any modifications. The stability of this new scheme is demonstrated by performing many thousands of iterations for a loss-free resonant structure.

III. THE NOVEL TIME INTERPOLATION

The commonly used leapfrog time-integration scheme can easily be applied to the new subgridding algorithm. Inside each grid, we perform a common time integration where the time step is limited by the well-known Courant–Levy stability criterion. The Courant–Levy criterion states that the maximum stable time step inside the CG and FG to be different by the

$$\frac{\partial H_{bcy}\left(i+\frac{1}{2},j,k+\frac{1}{2}\right)}{\partial t} = \frac{1}{\mu}\cdot\frac{1}{C_{Hbcy}}\left[\frac{EZJK - G_c E_z\left(i,j,k+\frac{1}{2}\right)}{\Delta x} - \frac{G_c E_x\left(i+\frac{1}{2},j,k+1\right) - G_c E_x\left(i+\frac{1}{2},j,k\right)}{\Delta z}\right] \tag{2}$$

$$\begin{aligned} EZJK = {} & g_1 E_{fz}\left(u,v-1,w-2+\frac{1}{2}\right) + g_2 E_{fz}\left(u,v,w-2+\frac{1}{2}\right) + g_3 E_{fz}\left(u,v+1,w-2+\frac{1}{2}\right) \\ & + g_4 E_{fz}\left(u,v-1,w-1+\frac{1}{2}\right) + g_5 E_{fz}\left(u,v,w-1+\frac{1}{2}\right) + g_6 E_{fz}\left(u,v+1,w-1+\frac{1}{2}\right) \\ & + g_7 E_{fz}\left(u,v-1,w+\frac{1}{2}\right) + g_8 E_{fz}\left(u,v,w+\frac{1}{2}\right) + g_9 E_{fz}\left(u,v+1,w+\frac{1}{2}\right) \\ & + g_{10} E_{fz}\left(u,v-1,w+1+\frac{1}{2}\right) + g_{11} E_{fz}\left(u,v,w+1+\frac{1}{2}\right) + g_{12} E_{fz}\left(u,v+1,w+1+\frac{1}{2}\right) \\ & + g_{13} E_{fz}\left(u,v-1,w+2+\frac{1}{2}\right) + g_{14} E_{fz}\left(u,v,w+2+\frac{1}{2}\right) + g_{15} E_{fz}\left(u,v+1,w+2+\frac{1}{2}\right) \end{aligned} \tag{3}$$

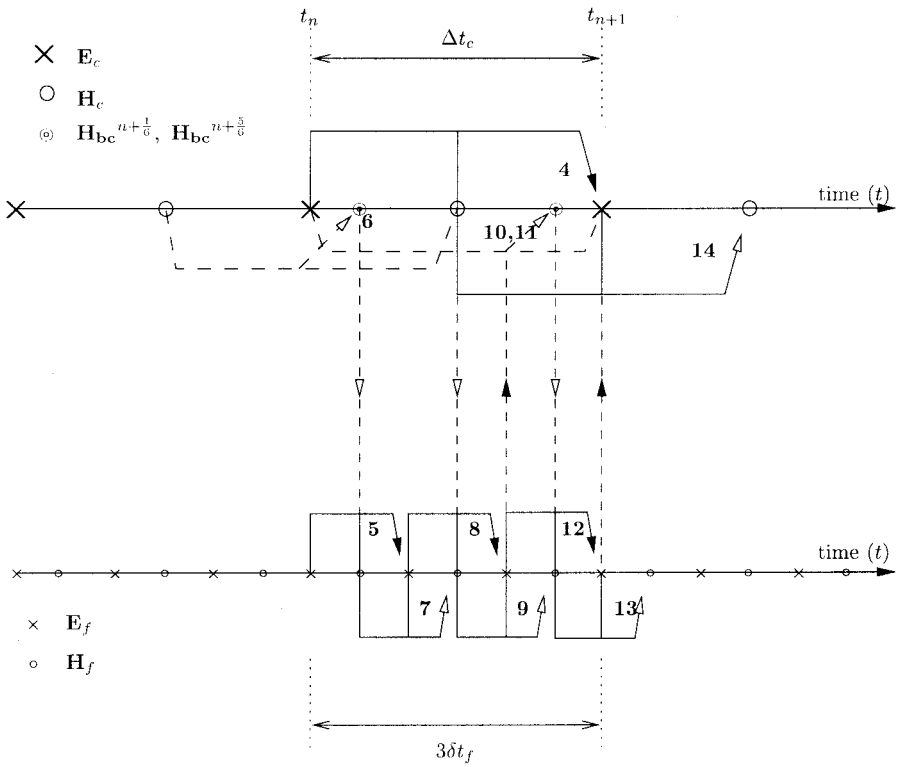

Fig. 6. The time-flow graph. Leapfrog time integration with novel time interpolation.

grid ratio, i.e., three. Maximum efficiency can be achieved by updating the fields in the FG three times while performing one time step in the coarse mesh. The boundary CG magnetic field is interpolated in time, between $H_{bc}^{n+(1/2)}$ and $H_{bc}^{n-(1/2)}$, to get the CG magnetic field at time $t = n+(1/6)$. This is used along with the existing FG magnetic field to update the boundary electric field at time $t = n + (1/3)$. The magnetic field at $t = n - (1/2)$ has to be stored to carry out this time interpolation. To calculate the boundary electric field at $t = n + 1$, we need the CG or FG magnetic field at $t = n + (5/6)$. However, this is not existing at the start of the iteration cycle. This is created by using the CG magnetic field at $t = n+(1/2)$, FG boundary electric field at $t = n + (2/3)$, and time interpolating the CG electric field at time $t = n + (2/3)$, as shown in the time-flow graph of Fig. 6. This newly created CG magnetic field is used to update the boundary electric field at time $t = n + 1$.

In this novel method, we have time interpolation of the magnetic field once and the electric field once in which the time reciprocity of interpolation has been taken care of automatically. The time-integration steps are schematically explained in the time-flow graph shown in Fig. 6. This procedure yields the following stable and efficient algorithm presented in Section IV.

IV. The Algorithm

We propose a new algorithm in this section. Its stability and accuracy is demonstrated for 3-D problems. The steps involved in the algorithm is succinctly explained with the aid of the time-flow graph shown in Fig. 6 along with a set of 15 steps [see (4)–(14b)]. The leapfrog time-integration steps are shown in the time-flow graph (Fig. 6), which explains the algorithm in a succinct manner. The numbers on the time-flow diagram corresponds to the equation numbers. The equation numbers ending with "b" corresponds to the following boundary updates:

$$\boldsymbol{E}_c^{n+1} \Leftarrow \boldsymbol{E}_c^n, \boldsymbol{H}_c^{n+(1/2)}, \boldsymbol{H}_{bc}^{n+(1/2)} \tag{4}$$

$$\boldsymbol{E}_f^{n+(1/3)} \Leftarrow \boldsymbol{E}_f^n, \boldsymbol{H}_f^{n+(1/6)} \tag{5}$$

$$\boldsymbol{H}_{bc}^{n+(1/6)} \Leftarrow \left[\frac{2\boldsymbol{H}_{bc}^{n+(1/2)} + \boldsymbol{H}_{bc}^{n-(1/2)}}{3}\right] \tag{6}$$

$$\boldsymbol{E}_{bf}^{n+(1/3)} \Leftarrow \boldsymbol{E}_{bf}^n, \boldsymbol{H}_f^{n+(1/6)}, \boldsymbol{H}_{bc}^{n+(1/6)} \tag{6b}$$

$$\boldsymbol{H}_f^{n+(3/6)} \Leftarrow \boldsymbol{H}_f^{n+(1/6)}, \boldsymbol{E}_f^{n+(1/3)}, \boldsymbol{E}_{bf}^{n+(1/3)} \tag{7}$$

$$\boldsymbol{E}_f^{n+(2/3)} \Leftarrow \boldsymbol{E}_f^{n+(1/3)}, \boldsymbol{H}_f^{n+(3/6)} \tag{8}$$

$$\boldsymbol{E}_{bf}^{n+(2/3)} \Leftarrow \boldsymbol{E}_{bf}^{n+(1/3)}, \boldsymbol{H}_f^{n+(3/6)}, \boldsymbol{H}_{bc}^{n+(1/2)} \tag{8b}$$

$$\boldsymbol{H}_f^{n+(5/6)} \Leftarrow \boldsymbol{H}_f^{n+(3/6)}, \boldsymbol{E}_f^{n+(2/3)}, \boldsymbol{E}_{bf}^{n+(2/3)} \tag{9}$$

$$\boldsymbol{E}_{bc}^{n+(2/3)} \Leftarrow \left[\frac{2\boldsymbol{E}_{bc}^{n+1} + \boldsymbol{E}_{bc}^n}{3}\right] \tag{10}$$

$$\boldsymbol{H}_{bc}^{n+(5/6)} \Leftarrow \boldsymbol{H}_{bc}^{n+(1/2)}, \boldsymbol{E}_{bf}^{n+(2/3)}, \boldsymbol{E}_{bc}^{n+(2/3)} \tag{11}$$

$$\boldsymbol{E}_f^{n+1} \Leftarrow \boldsymbol{E}_f^{n+(2/3)}, \boldsymbol{H}_f^{n+(5/6)} \tag{12}$$

$$\boldsymbol{E}_{bf}^{n+1} \Leftarrow \boldsymbol{E}_{bf}^{n+(2/3)}, \boldsymbol{H}_f^{n+(5/6)}, \boldsymbol{H}_{bc}^{n+(5/6)} \tag{12b}$$

$$\boldsymbol{H}_f^{n+(7/6)} \Leftarrow \boldsymbol{H}_f^{n+(5/6)}, \boldsymbol{E}_{bf}^{n+1}, \boldsymbol{E}_f^{n+1} \tag{13}$$

$$\boldsymbol{H}_c^{n+(3/2)} \Leftarrow \boldsymbol{H}_c^{n+(1/2)}, \boldsymbol{E}_c^{n+1} \tag{14}$$

$$\boldsymbol{H}_{bc}^{n+(3/2)} \Leftarrow \boldsymbol{H}_{bc}^{n+(1/2)}, \boldsymbol{E}_c^{n+1}, \boldsymbol{E}_{bf}^{n+1}. \tag{14b}$$

The leapfrog time stepping can be described as follows (the numbers in the brackets corresponds to the above equations).

TABLE III
THE FIELD COMPONENTS AT THE START AND END OF THE ITERATION CYCLE

Start (n)	$\mathbf{E}_c^n$	$\mathbf{H}_c^{n+\frac{1}{2}}$	$\mathbf{E}_{bf}^n$	$\mathbf{H}_{bc}^{n+\frac{1}{2}}$	$\mathbf{E}_f^n$	$\mathbf{H}_f^{n+\frac{1}{6}}$
End (n+1)	$\mathbf{E}_c^{n+1}$	$\mathbf{H}_c^{n+\frac{3}{2}}$	$\mathbf{E}_{bf}^{n+1}$	$\mathbf{H}_{bc}^{n+\frac{3}{2}}$	$\mathbf{E}_f^{n+1}$	$\mathbf{H}_f^{n+\frac{7}{6}}$

Step 1) Update the CG electric field (4).
Step 2) Update the FG electric field (5).
Step 3) Do the time interpolation of the CG boundary magnetic field to get the CG field at FG time interval, $t = n + 1/6$. Note that the CG magnetic field is not available at the FG interval at the beginning (6).
Step 4) Update the FG boundary electric-field components by utilizing the CG magnetic field that was calculated in Step 3 (5b).
Step 5) Update the FG magnetic field (7).
Step 6) Update the FG electric field (8).
Step 7) Update the FG boundary electric field using the space interpolated CG boundary magnetic field. Note that no time interpolation is required at this time level (8b).
Step 8) Update the FG magnetic field (9).
Step 9) This time, do the time interpolation of the CG boundary electric field to obtain CG boundary electric the field at time, $t0 = n + 2/3$ (10).
Step 10) Create the CG boundary magnetic field at time $t = n + 5/6$ using the FG and CG electric-field components. Here, the CG electric-field components are those obtained in Step 9 (11).
Step 11) Update the FG electric field (12).
Step 12) Update the FG boundary electric-field components by utilizing the CG magnetic field that was obtained in Step 10 (12b)..
Step 13) Update the FG magnetic field (13).
Step 14) Update the CG magnetic field (14).
Step 15) Update the CG boundary magnetic field (14b).
Step 16) Cycle.

The starting and ending field iterations are tabulated in Table III, which shows the fields that are available at the start and end of one cycle.

V. NUMERICAL RESULTS

In order to demonstrate the stability and accuracy of this new scheme, 3-D problems are selected such that there will be a field gradient in one, two, and finally, three directions. These problems fully represent the general complexity that the FDTD method came across. We have applied a 3-D version of this algorithm to calculate the resonant frequencies of arbitrarily filled inhomogeneous resonators (Fig. 7) and a finline resonator (Fig. 8). The SG covers the dielectric block and extends by one CG in each direction. The results for the case $\Delta x = \Delta y = \Delta z = 90$ cm have been compared using a CG only, FG only and coarse FG's i.e., the SG in Table IV. The results from the SG agrees very well with FG results

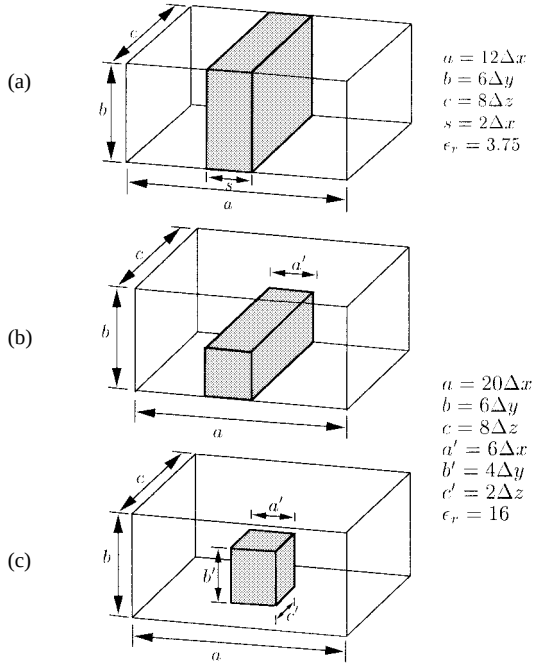

Fig. 7. 3-D inhomogeneous resonators analyzed.

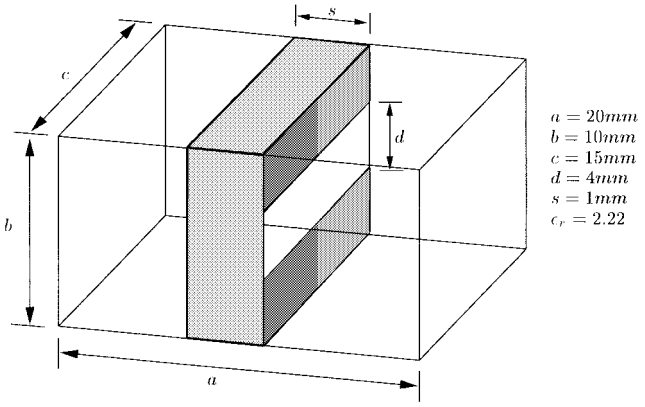

Fig. 8. Finline cavity.

and are shown in Table IV. Runtimes, using an unoptimized code, for the FG and SG were 56 and 47 min, respectively. It is expected that greater savings in computer time would be obtained if the code were optimized.

In order to ascertain the disturbance caused to a wave propagating through a uniform waveguide in which a subgridded region has been included, the following test was carried out. A parallel-plate waveguide having a width of 16.2 mm, height of 10.8 mm, and length of 180 mm was considered. The SG region dimensions are 7.2 × 3.6 × 9 mm and is centrally located such that all six interface reflections can be observed. The coarse spatial step is 0.9 mm and the grid ratio is three. Magnetic-wall boundary conditions were applied to the sides of the waveguide and electric-wall boundary conditions were applied to the top and bottom. The guide was made long enough so that the ABC's at the ends did not affect the results. Fig. 10 shows the reflection coefficient for the TEM mode, which can be seen to be less than −30 dB for frequencies up to 20 GHz.

TABLE IV
RESONANT FREQUENCIES OF ARBITRARILY FILLED DIELECTRIC RESONATORS

Fig. No	s/a	CG(MHz)	FG(MHz)	SG(MHz)
7a	1/6	17.59	17.39	17.39
	1/3	14.79	14.69	14.69
7b		8.99	8.79	8.79
7c		13.89	13.69	13.69
8		10.84 GHz	10.74 GHz	10.73 GHz

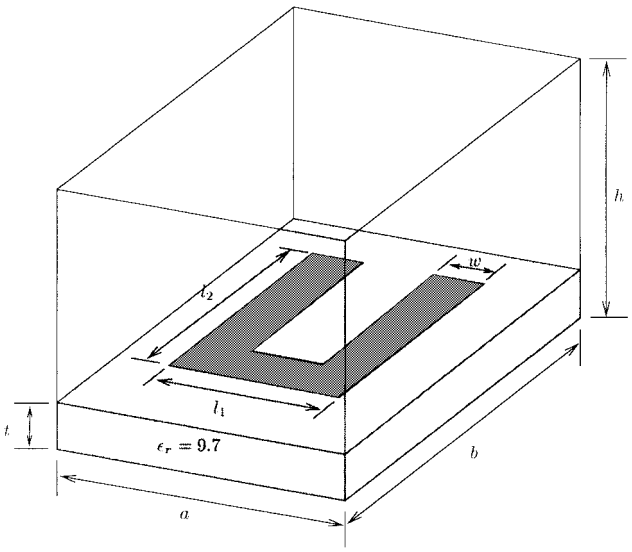

$a = b = 10.8\text{mm}$, $h = 12.7\text{mm}$
$l_1 = l_2 = 6\text{mm}$, $w = 1.5\text{mm}$, $t = 1.27\text{mm}$

Fig. 9. Hairpin resonator.

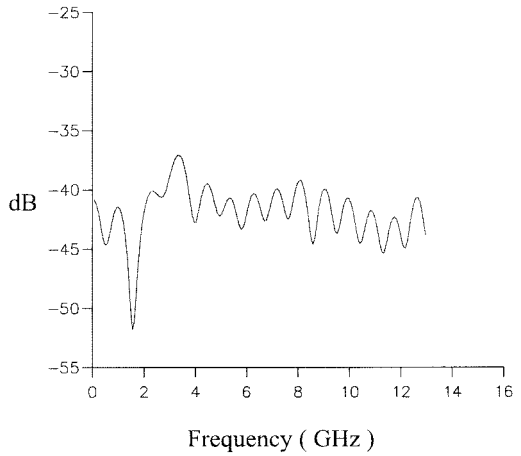

Fig. 10. Reflections in a parallel-plate guide with a subgridded region in a homogeneous section of line. The SG is centrally located in the waveguide.

TABLE V
RESONANT FREQUENCY OF HAIRPIN RESONATOR CALCULATED USING CG ONLY, FG ONLY, AND BOTH

Fig. No	CG(GHz)	FG(GHz)	SG(GHz)
9	4.140	4.445	4.475

Finally a hairpin resonator, shown in Fig. 9, is analyzed. The dimensions used are: 1) $a = b = 10.8$ mm; 2) $l_1 = l_2 = 6$ mm; 3) $w = 1.5$ mm; 4) $t = 1.27$ mm and 5) $h = 12.7$ mm. In this case, the FG also encloses the metallization in all directions by one CG. It can be seen from Table V that the resonance frequency calculated using an SG and FG is in excellent agreement. The runtime for the SG was 1200 min and the memory used was 670 kbytes, whereas for the FG solution, the runtime was 14000 min and the memory requirement was 5.67 Mbytes.

VI. CONCLUSIONS

We have presented a stable subgridding algorithm with a novel time interpolation. We have implemented this algorithm in three dimensions to demonstrate its stability and accuracy in dealing with three practical applications. One is to characterize arbitrarily filled dielectric waveguide and the others are the calculation of resonance frequencies of the arbitrarily filled dielectric resonators, fine-line resonator, and hairpin resonator. We have showed that the 3-D discontinuities can be modeled accurately and efficiently.

ACKNOWLEDGMENT

The authors thank Prof. J. McGeehan for provision of facilities in the Centre for Communications Research, University of Bristol, Bristol, U.K. The authors also thank Dr. I. Craddock for helpful discussions.

REFERENCES

[1] K. S. Yee, "Numerical solution of initial boundary value problems involving Maxwell's equations in isotropic media," *IEEE Trans. Antennas Propagat.*, vol. AP-14, pp. 302–307, Apr. 1966.
[2] A. Taflove and M. E. Brodwin, "Numerical solution of steady-state electromagnetic scattering problems using the time-dependent Maxwell's equations," *IEEE Trans. Microwave Theory Tech.*, vol. MTT-23, pp. 623–630, Aug. 1975.
[3] A. Taflove, K. R. Umashankar, B. Beker, F. Harfoush, and K. S. Yee, "Detailed FDTD analysis of electromagnetic fields penetrating narrow slots and lapped joints in thick conducting screens," *IEEE Trans. Antennas Propagat.*, vol. 36, pp. 247–257, Feb. 1988.
[4] D. M. Sheen, S. M. Ali, M. Abouzahra, and J. A. Kong, "Application of the three-dimensional finite-difference time-domain method to the analysis of planar microstrip circuits," *IEEE Trans. Microwave Theory Tech.*, vol. 38, pp. 849–857, July 1990.
[5] X. Zhang and K. K. Mei, "Time-domain finite difference approach to the calculation of the frequency-dependent characteristics of microstrip discontinuities," *IEEE Trans. Microwave Theory Tech.*, vol. 36, pp. 1775–1787, Dec. 1988.
[6] K. S. Kunz and R. J. Luebbers, *Finite Difference Time Domain Method for Electromagnetics*. Boca Raton, FL: CRC Press, 1993.
[7] A. Taflove, *Computational Electrodynamics: The Finite Difference Time Domain Method*. Norwood, MA: Artech House, 1995.

[8] J. G. Maloney and G. S. Smith, "The use of surface impedance concept in the FDTD Method," *IEEE Trans. Antennas Propagat.*, vol. 40, pp. 38–48, Jan. 1992.
[9] T. G. Jurgens, A. Taflove, K. Umashankar, and T. G. Moore, "Finite-difference time-domain modeling of curved surfaces," *IEEE Trans. Antennas Propagat.*, vol. 40, pp. 357–366, Apr. 1992.
[10] J. H. Beggs, R. J. Luebbers, K. Yee, and K. S. Kunz, "FDTD implementation of surface impedance boundary conditions," *IEEE Trans. Antennas Propagat.*, vol. 40, pp. 49–56, Jan. 1992.
[11] K. Umashankar, A. Taflove, and B. Bekar, "Calculation and experimental validation of induced currents on coupled wires in an arbitrary shaped cavity," *IEEE Trans. Antennas Propagat.*, vol. AP-35, pp. 1248–1257, Nov. 1987.
[12] C. J. Railton, I. J. Craddock, and J. B. Schneider, "Improved locally distorted CPFDTD algorithm with provable stability," *Electron. Lett.*, vol. 31, pp. 1585–1586, Aug. 1995.
[13] ———, "Analysis of general 3D PEC structures using an improved CPFDTD algorithm," *Electron. Lett.*, vol. 31, pp. 1753–1754, Sept. 1995.
[14] I. S. Kim and W. J. R. Hoefer, "A local mesh refinement algorithm for the time domain-finite difference method using Maxwell's curl equations," *IEEE Trans. Microwave Theory Tech.*, vol. 38, pp. 812–815, June 1990.
[15] S. S. Zivanovic, K. S. Yee, and K. K. Mei, "A subgridding method for the time-domain finite-difference method to solve Maxwell's equations," *IEEE Trans. Microwave Theory Tech.*, vol. 39, pp. 471–479, Mar. 1991.
[16] D. T. Prescott and N. V. Shuley, "A method for incorporating different sized cells into the finite-difference time-domain analysis technique," *IEEE Microwave Guided Wave Lett.*, vol. 2, pp. 434–436, Nov. 1992.
[17] S. Xiao, R. Vahldieck, and H. Jin, "A fast two dimensional FDTD full-wave analyzer with adaptive mesh size," in *IEEE MTT-S Symp. Dig.*, 1992, pp. 783–786.
[18] K. M. Krishnaiah and C. J. Railton, "Passive equivalent circuit of FDTD: An application to subgridding," *Electron. Lett.*, vol. 33, pp. 1277–1278, July 1997.
[19] P. Thoma and T. Weiland, "A consistent subgridding scheme for the finite difference time domain method," *Int. J. Numer. Modeling*, vol. 9, pp. 359–374, 1996.
[20] M. Okoniewski, E. Okoniewska, and M. A. Stuchly, "Three-dimensional subgridding algorithm for FDTD," *IEEE Trans. Antennas Propagat.*, vol. 45, pp. 422–429, Mar. 1997.
[21] C. R. Brewitt-Taylor and P. B. Johns, "On the construction and numerical solution of transmission line and lumped network models of Maxwell's equations," *Int. J. Numer. Methods Eng.*, vol. 13, no. 1, pp. 13–30, 1980.
[22] I. J. Craddock and C. J. Railton, "Application of a circuit-based approach to ensuring the stability of modified finite difference time domain algorithms," in *Proc. 12th Int. Zurich EMC Symp. Dig.*, Feb. 1997, pp. 515–518.
[23] I. J. Craddock, C. J. Railton, and J. P. McGeehan, "Derivation and application of a passive equivalent circuit for the finite difference time domain algorithm," *IEEE Microwave Guided Wave Lett.*, vol. 6, pp. 40–42, Jan. 1996.

K. M. Krishnaiah, photograph and biography not available at the time of publication.

Chris J. Railton (M'88) received the B.Sc. degree in physics with electronics from the University of London, London, U.K., in 1974, and the Ph.D. degree in electronic engineering from the University of Bath, Bath, U.K., in 1988.

From 1974 to 1984, he worked in the scientific civil service on a number of research and development projects in the areas of communications, signal processing and electromagnetic compatibility (EMC). From 1984 to 1987, he was with University of Bath, where he was involved in the mathematical modeling of boxed microstrip circuits. He is currently with the Centre for Communications Research, University of Bristol, Bristol, U.K., where he leads the Computational Electromagnetics Group, which is involved in the development of new algorithms and their application to monolithic microwave integrated circuits (MMIC's), planar antennas, optical waveguides, microwave and radio frequency (RF) heating, EMC, and high-speed logic.